Scientific Visualization, 2025, volume 17, number 1, pages 138 - 149, DOI: 10.26583/sv.17.1.11

On The Visualization of Subattractor Under Mixed Tidal Forcing

Stepan Elistratov[1,A,B,C], Ivan But[2,B]

[A] Shirshov Institute of Oceanology of RAS, Moscow, Russia
[B] Ivannikov Institute for System Programming of RAS, Moscow, Russia
[C] Sobolev institute of mathematics of Siberian branch of RAS, Novosibirsk, Russia

[1] ORCID: 0000-0002-7006-6879, sa.elist-ratov@yandex.ru
[2] ORCID: 0000-0001-5915-0941, ivan.but@ispras.ru

Abstract

One of the principle conditions of a wave attractor appearance is a periodic external forcing. Real forcing in natural basins caused by tidal interaction is more complex than a monochromatic which is usually used in internal wave attractors investigations. Multi-frequency forcing may lead to the multiple wave attractor formation, some of them may be of low energy, which affects their detection. In the article we simulate a mixed forcing for an internal wave attractor flow and visualize subattractor formed due to this forcing type using several methods, including Proper Orthogonal Decomposition. It is shown that the latter method reveals sub-attractor even in case of highly turbulent flow.

Keywords: wave attractor, mixed tides, visualization, POD.

1. Introduction

Wave attractor is a peculiar phenomenon of internal and/or inertial wave self-focusing in stratified/rotating fluid in a specific geometry. The main feature is that instead of standing modes there are running waves in the closed domain leading to the waves' energy accumulation. The necessary conditions for internal wave attractors appearance are: a slope, periodic external forcing and vertical stratification [1]. Since their discovery in 1995 they were thoroughly studied both experimentally [2, 3, 4, 5, 6, 7, 8, 9, 10] and numerically [11, 12, 13, 9, 14, 15, 16, 17]. The comparison shows [11, 18] that both methods yield quite close results, which allows the numerical simulation to be widely used for investigation of wave attractors flows. Field observations managed to detect a natural attractor [19, 20]; its numerical reproduction [21] verified the approach used for numerical simulations. The issues of the wave attractor detection are connected with the energy overpumping [22] into a basin which turbulizes the flow making an attractor hidden beyond the turbulence. However, even invisible, an attractor can radically affect the flow and kinetic energy accumulation [16], and hence be itself a source of turbulence.

The mechanism of internal wave attractors formation lies in a specific dispersion relation which caused by the vertical stratification [1]:

$$\frac{\omega}{N} = \cos\theta, \tag{1}$$

where $N = \sqrt{-\frac{g}{\rho}\frac{\partial \rho}{\partial y}}$ is a buoyancy frequency, ω — wave beam frequency, θ — angle with the vertical direction. The dispersion relation does not depend on the wave number on the frequency only, yielding the reflection law that conserves angle with vertical axis (along the gravity) rather than incidence-reflection angle. In terms of numerical simulation it can be used for attractor prediction at the given frequency. However, it should be noticed that equation (1)

was derived for inviscid linear liquid (omitting quadratic convective and viscous parts in Navier-Stokes equation), and the figure obtained by this method should be considered as an attractor's "skeleton", whereas the non-linear nature of the Navier-Stokes equation will have an impact as a turbulence.

The most of works on the attractors were concentrated on monochromatic external forcing hence it originates from the tidal interaction that is sine-like, despite both the experimental setups [23] and numerical simulation allow to provide a wide range of external forcing on the system. To study how the tide shape can influence on the attractor flow we chose mixed semidiurnal tides [24, 25, 26, 27, 28] that have different height of low end high tides (minima and maxima of the sea level, see further Fig. 2). While the simulation we will set the forcing in an approximated form representing the main features of this tide type.

As the forcing is not monochromatic, there is an option for the appearance of sev-eral attractors simultaneously. The non-monochromatic forcing for two close external force frequencies for an attractor flow was studied in [29], where such a possibility was verified; in that investigation the intensiveness of sine forcing modes was of the same order without any link to the real tide form for the biharmonic attractor be clearly seen. In our case, minor forcing harmonics will have lower amplitude than the main one, and the attractor forming on one of them will be hardly distinguishable in the presence of the main structure. To reveal it, several methods will be used and compared.

2. Numerical setup

The problem is solved in 2D setup following [18, 11, 12] to save computational resources; for the domain an orthogonal trapezium was used as represented on Fig. 1. This geometry fully satisfies the attractor formation requirements [1] and is widely used for attractor studies [12, 9, 15].

Another necessary condition is a periodic forcing [1]; in nature it is tidal force, but experimentally it is provided by a wave maker [23] producing a border periodic perturbation in a given shape by a system of shafts and eccentrics [30, 31]. Following the experiment we use the latter approach; in our problem the wave maker is situated on the top side since its position is not crucial [32, 17].

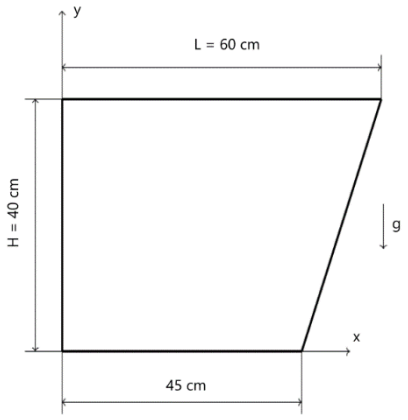

Figure 1: Problem domain

The equation system to be solved consists of the following: Navier-Stokes equation in Boussinesq approximation

$$\frac{\partial \vec{v}}{\partial t} + (\vec{v}, \nabla)\vec{v} = -\frac{1}{\rho_m}\nabla \tilde{p} + \frac{\rho_s}{\rho_m}\vec{g} \tag{2}$$

salt transition equation:

$$\frac{\partial \rho_s}{\partial t} + (\vec{v}, \nabla)\rho_s = \lambda_s \rho_s \tag{3}$$

$$\rho = \rho_m + \rho_s \tag{4}$$

and continuity equation (for incompressible flow):

$$\operatorname{div} \vec{v} = 0 \tag{5}$$

where $\tilde{p}$ is a pressure without its hydrostatical part $g\rho_m$, ρ_m is a fresh water density, ρ_s — dissolved salt density, λ_s is a salt diffusivity.

In what follows x-axis is directed along the lower trapezium base, y — vertically (Fig. 1).

The gravity is against the y-axis.

Wave maker as it was said above is on the top side; hence its influence will be de-scribed as the upper border condition. The mixed semidiurnal tide is introduced as a sine with an envelope oscillating on a half frequency:

$$s(x,t) = a \sin(\omega_0 t) \sin(2\pi x/L) \tag{6}$$

where $s(x)$ is an upper border profile, a is a forcing amplitude and ω_0 is a particular frequency; α_a governs the difference between low and high tides. Such a shape of the profile was selected to represent the main properties of the mixed semidiurnal tide – two high and two low tides with different heights, as seen on Fig. 2.

Small forcing amplitude respectively the domain size allows to rewrite upper boundary profile condition (6) into a form of a velocity condition and to solve the problem in a constant-shape domain:

$$\begin{aligned} \vec{v}|_{y=H} &= \dot{s}(x,t)\vec{e}_y \\ &= a\omega_0 \sin(2\pi x/L)[\cos(\omega_0 t) - 1.5\alpha_a \cos(1.5\omega_0 t) + 0.5\alpha_a \cos(0.5\omega_0 t)]\vec{e}_y \end{aligned} \tag{7}$$

On the other borders we set $\vec{v}|_b = 0$.

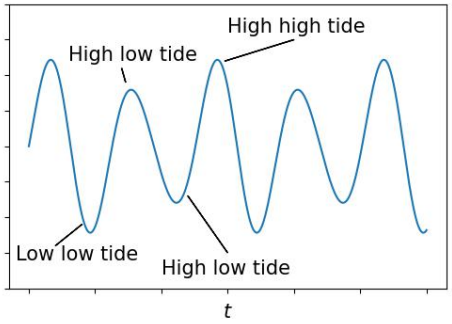

Figure 2: Tide profile (6) principal shape

For the salinity the impermeability condition $\partial\rho/\partial n = 0$ was used on all theboundaries.

The initial salinity distribution was linear:

$$\rho_m|_{t=0} = g_m(H - y),$$

smoothed in the near-border regions in order to satisfy the impermeability condition. g_m ('g' for 'gradient') was selected form the buoyancy frequency N (which is constant in case of linear profile):

$$g_m = N^2 \frac{\rho_m}{g}$$

In our case we used $N = 1$ s^{-1}.

Hence external force is periodic, we introduce a non-dimensional time t/T_0 ($T_0 = 1/f_0$, $f_0 = \omega_0/(2\pi)$). Also we will refer to attractors in (n,m) notation following [2], implying the attractor hasn reflection from horizontal and m from sides (vertical/slope).

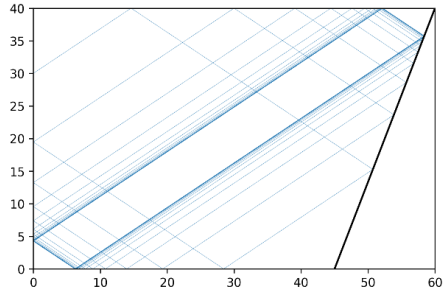

Figure 3: Ray tracing, $\omega = \omega_0$

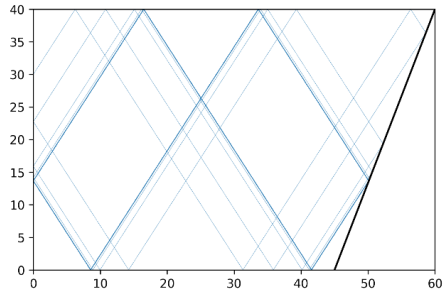

Figure 4: Ray tracing, $\omega = 1.5\,\omega_0$

As the presence of two attractor simultaneously is wanted, they can appear only on different frequency. Boundary perturbation in form (6) provides triple frequency forcing; thus, attractors will appear on some of these frequencies.

To select basic frequency ω_0 properly (i.e. so that either $0.5\omega_0$ or $1.5\omega_0$ has also an attractor) we ran ray-tracing procedure [2] which predicts internal wave beams propagation basing on the dispersion relation (1). It was found that for $\omega_0 = 0.565$ s^{-1} there is an (1,1) attractor and on $1.5\omega_0 = 0.8475$ s^{-1} there is (2,1). We remind that an (n,m)-type attractor is that withn horizontal beam reflections and m vertical ones.

Despite ray-tracing prediction, it should be taken into account that, first, it derives from dispersion relation that omits non-linear effects, and second, real liquid is viscous that tends to widen attractor beams as $\propto \nu^{1/3}$ [32]. For this reason we simulate a strictly unturbulent ("laminar") flow regime with small external force amplitude ($a_0 = 0.0001$ cm) in liquid with reduced viscosity (1000 times less than real water, i.e. 1×10^{-5} cm^2/s). Such small parameters in numerical experiment are justified hence real attractors are subject to scale effects [32] which are regulated by domain sizes and viscosity.

After the external frequency determination we ran numerical simulation. The problem was solved using spectral element package *Nek5000* [33] providing high order of accuracy on a 48x48 spectral element grid with constant time step following [34, 35]. For the post-processing *python3* was utilized.

3. Numerical simulation and POD decomposition

3.1. Computational results

Fig. 5 shows vertical velocity component v_y spatial distribution in steady attractor regime. The main (1,1) attractor is clearly visible and corresponds the ray-tracing pre-diction (Fig. 3); along with it there is another (2,1) attractor visible on the background. Its shape reminds the structure from Fig. 4, but its intensiveness is much lower than that of the main attractor. As the external forcing amplitude was small, the flow is almost unturbulent which is the point why the substructure is visible. If we has simulated the turbulence would be much greater, which could perturb even the main attractor structure [36, 16, 17] — in such case the subatractor will be hardly distinguishable on a turbulent background and would require additional tools for extraction and visualization (as we will show below).

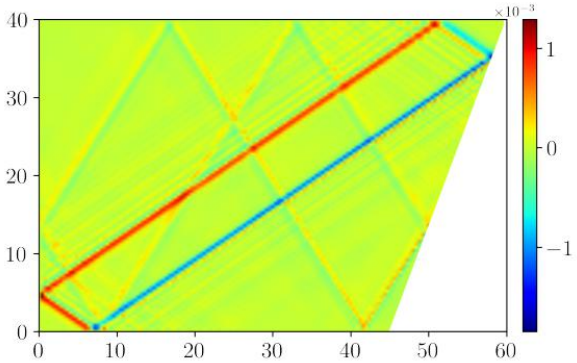

Figure 5: v_y snapshot, $t = 200T_0$

Before we immerse ourselves into substructure visualization issues in order to take a closer look at the flow regime formed it is reasonable to consider the kinetic energy given by a formula:

$$E = \frac{1}{2}\int \rho v^2 dV \tag{8}$$

As in this form energy will depend on external force amplitude and frequency as well as on the vessel volume even in the absence of scale effects, it is reasonable to consider the following value called relative kinetic energy:

$$\bar{E} = E/E_w, \qquad E_w = {}^1\!/_2\, a^2\omega_0^2 M, \tag{9}$$

where $M = \int \rho dV$ is a full water mass. Wherein E_w has a physical sense of the energy amplitude of a vessel oscillating with the same amplitude and frequency with a tank as a rigid body.

The interesting feature of this multi-attractor flow is the kinetic energy temporal behaviour. Usually laminar attractors have steadifying time of $\sim 30T_0$ for this geometry type [16], but here is a range $20T_0 - 150T_0$ of "slow growth" of the energy (slow comparatively with conventional sharp growth, as in the very beginning, at $0 - 10T_0$). It is known that (n,1) attractors steadifying time grows proportionally to n [37], and subattractor is of (2,1) type while the main attractor is (1,1); howbeit, it can hardly explain the energy behavior hence the subattractor energy is more than 10 times less than that of the main structure (see section 3.3, Fig. 12-13).

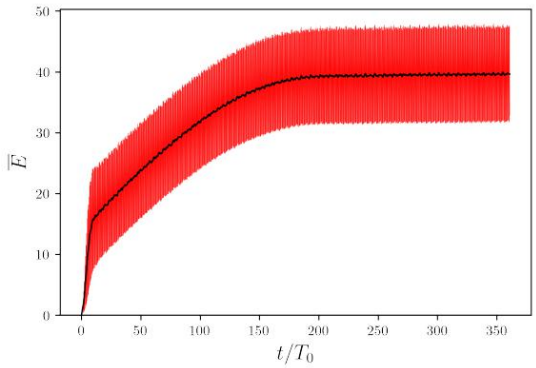

Figure 6: Unusual behaviour of relative kinetic energy

To comprehend the multi-frequency attractor behavior we calculated v_y spectrum (Fig. 7). The temporal spectrum was made for steady attractor regime, $200T_0 - 350T_0$ and averaged over a square vicinity of the point x = 30 cm, y = 25 cm situated on a main attractor beam near that of the subattractor. The spectrum plotted on Fig. 7 has main peak of f_0 corresponding the main (1,1) attractor, triadic resonance instability peaks and minor forcing peaks $0.5f_0$ and $1.5f_0$. The latter two have different height, hence the second one corresponds to the sub-

attractor and accumulates energy (not at the same rate as the main attractor, the accumulation is sufficient) — while $0.5f_0$ does not form an attractor and hence does not accumulate energy as on $1.5f_0$. The instability peak on the left ($\sim 0.42f_0$) turns out to be even higher because its mother wave is that of f_0 with the maximum energy.

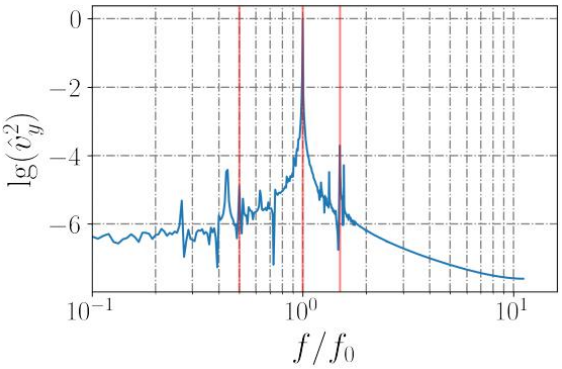

Figure 7: v_y spectrum. Triple frequencies are marked red

3.2. Spectrum filtration

As soon as the subattractor exists on its own frequency $1.5f_0$, it seems reasonable that the attractor can be visualized by frequency filtration.

The procedure is following: one make a Fourier transform of the flow over the time axis, multiplies by a filter function and finishes with inverse Fourier transform:

$$u_f = FFT^{-1}\left(W(\omega)FFT\,(u)\right),$$

where u is a function to filter, u_f — filtration result, $W(\omega)$ — window function.

To obtain subattractor the filtration should be made over $1.5f_0$. The symmetric round-box filter was used in order not to widen the spectral peak; although using spe-cial filters like Hanning, Blackmann or Batrlett (triangle) window did not influence the result. As the minor external force peaks are weak, they can be interfered by the bearing instability (see Fig. 7); thus the filter should be narrow enough. In this particular case its width was 0.011 Hz, or $0.13f_0$. It is the maximum width for clear subattractor visibility; the wider filtration leads to the interference with the main attractor.

Fig. 8 shows the filtered spectrum part with the whole spectrum on the background. The spectrum was made over the steady regime time range, $200T_0$–$350T_0$. The subattractor filtered is visible on fig. 9.

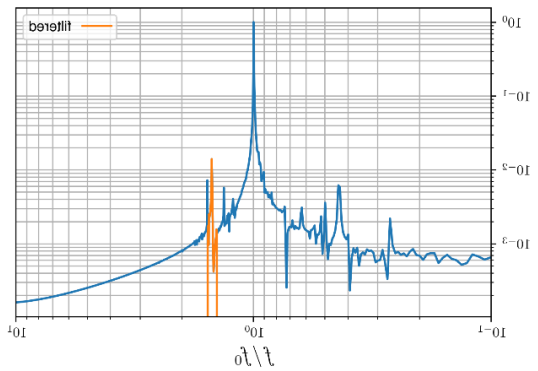

Figure 8: Spectrum and its filtered part over $1.5f_0$

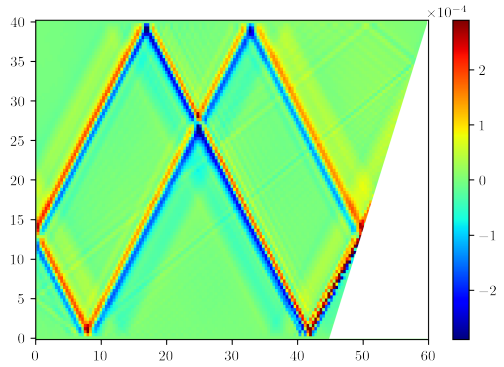

Figure 9: Flow filtered over $1.5f_0$

Despite the suitable result, this method can be more complicated in real investigations. Subattractor's spectral peaks are distinguishable but can be confused with turbulent ones and require to now their exact position. Here, we simulated a qualitative form of the tide and knew in advance where the additional peaks will be. Real tide is usually more complex, and tidal modes may not be so monochromatic, which complicates the problem of subattractors identification.

3.3. POD

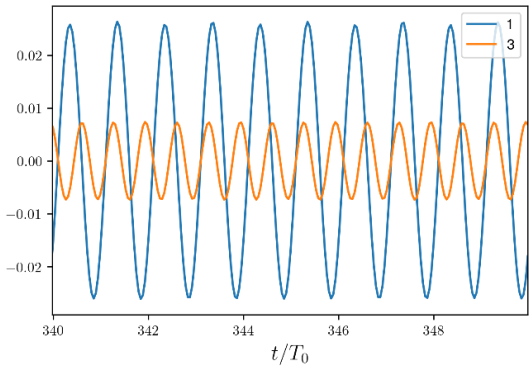

Figure 10: selected POD coefficients

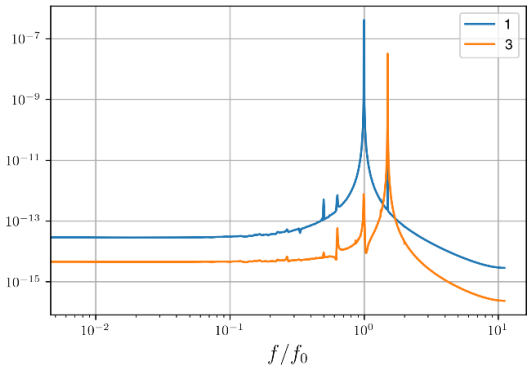

Figure 11: Selected coefficients spectrum

Another way for subattractor detection is a POD decomposition modes. We used POD decomposition [38] that represents the flow data as follows:

$$u(t,x,y) \approx \sum_j \Phi_j(x,y)T_j(t)$$

Herewith Φ_j functions are called spatial modes, T_j — temporal coefficients. The modes gathered will be spatially orthogonal, which make the decomposition to be an analogue of Fourier decomposition with automatic basis selection.

To obtain an adequate result the decomposition requires enough time slices (snap-shots). In the problem considered it was made over a steady-attractor time range, $200T_0$– $350T_0$, with 3336 snapshots.

First two POD modes correspond the main attractor on frequency f_0. It is two modes (Fig. 12) hence there are travelling waves on the attractor, and a travelling wave is de-composed into two modes. Their temporal coefficients have the same spectra but shifted on $\pi/2$ by phase, thus we plot only one of them (Fig. 10). However, their energies slightly differ because of presence of the standing component on the same frequency (there is a standing way component which is proved by energy oscillation, Fig. 6).

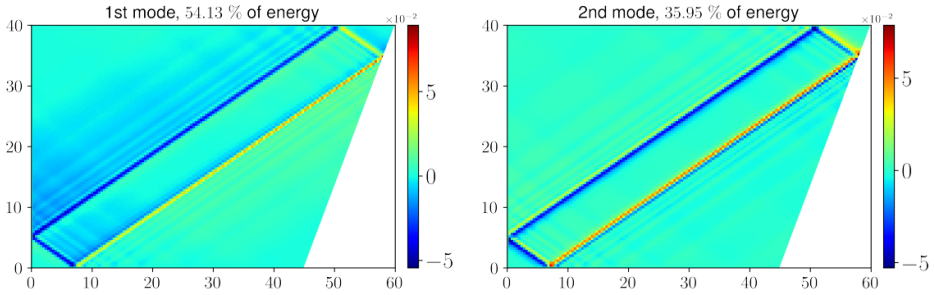

Figure 12: First two POD modes: the main attractor

POD decomposition allows to observe a subattractor formed on $1.5f_0$ frequency on Fig. 13. It has very low energy but still can be visible on the flow snapshots (see Fig. 5, background). The corresponding temporal coefficient spectrum has a peak on $1.5f_0$ which means that subattractor frequency is automatically substracted. We emphasize that we did not take any steps for the selection of subattractor mode specially on a particular frequency, it was determined by the algorithm.

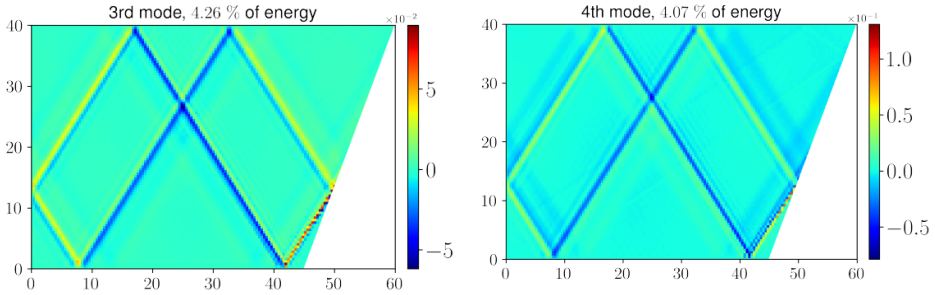

Figure 13: POD modes: the subattractor

In order to illustrate that POD successes the extraction visualizable subattractor not only in laminar case we made a decomposition for a turbulent case ($a = 0.07$ cm). Fig. 14 shows the typical v_y snapshot and two attractor modes extracted from the complex flow.

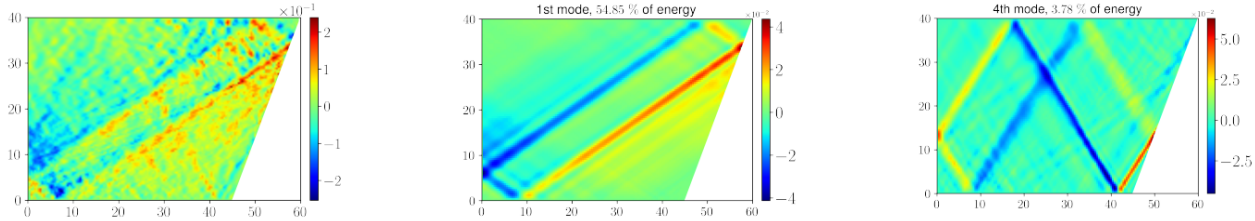

a b c

Figure 14: Turbulent case: v_y slice (a), attractor (b) and subattractor (c) modes

As follows from [16], if the attractor is not visible it does not mean it is immaterial. In order to more illustrate the capability of the POD-based visualization we provide here the illus-

tration of the extremely low-energy attractor. We simulate the flow with ω_0 = 0.419 s^{-1}, so that there is no attractor at the ω_0 and (1,1) attractor at $1.5\omega_0$ = 0.628 s^{-1}, with very low α_a = 0.01 just to test if POD manage to recover (1,1) attractor mode. Additionally we complicates the detection by adding some turbulence (a = 0.02 cm). The resulting flow is rather turbulent (see Fig. 15(a)); however, there is a mode in POD shown on Fig. 15(b) with clearly visible (1,1) attractor. This testifies that such tool is capable to reveal deeply-hidden attracttor subflow even with low energy and can be successfully used for attractor detection.

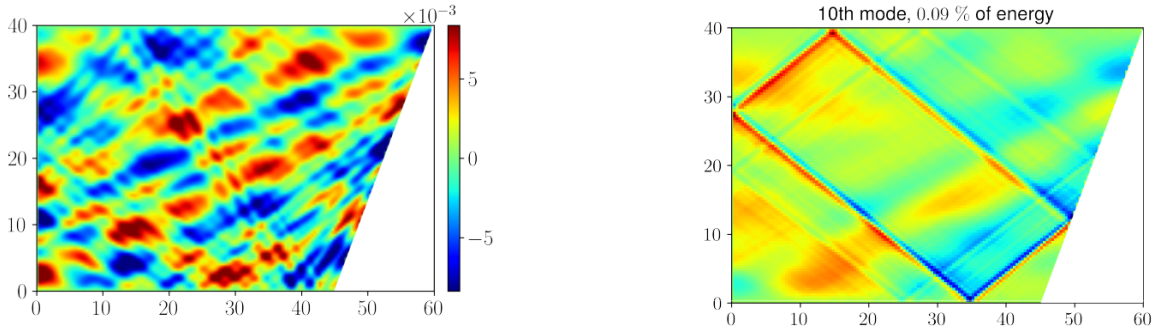

a b

Figure 15: Low-energy attractor: v_y slice (a) and the attractor extracted by POD (b)

Such approach may be useful in the area of real-basin attractor searching. Nowadays methods like deep-sea PIV [39, 40, 41] allow to obtain a simultaneous snapshot of a give plane. A set of such snapshots can be analysed to detect coherent structure like wave attractors. The present study shows that POD processing of a snapshot series may detect coherent structures of low enough intensiveness without special fitting.

Also it may be helpful in internal and inertial wave attractor experimental study where PIV is wide-spread [42, 43, 44] and experimental setups can be finely calibrated for comprehensive study of low-energy coherent structures.

4. Conclusions and Discussions

Wave attractor flows are capable to have additional subattractor structures if the forcing is non-monochromatic. The structures formed under mixed-tide condition may carry lower energy than the main structure and hence be hard to extracted. However, such subattractor in turbulent regimes becomes an additional source of instability and shall be taken into account.

Such subattractors form on one of the forcing harmonic's frequency. It is shown that if the frequencies are known, substructure can be visualized using spectral filtering. However, the procedure is slow and requires a fine tuning (which worthies it if the frequency is determined) and a narrow enough filter use. The detection problem significantly complicates if the forcing sub-harmonics are poorly defined, which can occur in case of experimental data studying.

As an alternative, POD decomposition can be used for a subattractor visualization. The method does not require special tuning and can be use on unprepared data. De-spite the low energy, subattractor is effectively shown up without special efforts; its frequency will be defined automatically. This method is recommended for applying on experimental data, noised data or in case of multi-frequency forcing.

References

1. Leo Maas and Frans-Peter A Lam. Geometric focusing of internal waves. Journal of Fluid Mechanics, 300:1–41, 1995.

2. L. R. M. Maas, D. Benielli, J. Sommeria, and F.-P. A. Lam. Observation of an internal wave attractor in a confined, stably stratified fluid. Nature, 388:557–561, August 1997.

3. Leo R. M. Maas. Wave focusing and ensuing mean flow due to symmetry breaking in rotating fluids. Journal of Fluid Mechanics, 437:13–28, 2001.
4. Astrid Manders and Leo Maas. Observations of inertial waves in a rectangular basin with one sloping boundary. Journal of Fluid Mechanics, 493:59–88, 2003.
5. Leo R.M. Maas. Exact analytic self-similar solution of a wave attractor field.Physica D: Nonlinear Phenomena, 238(5):502–505, 2009.
6. Jeroen Hazewinkel, Pieter Van Breevoort, Stuart B Dalziel, and Leo Maas. Observations on the wavenumber spectrum and evolution of an internal wave attractor. Journal of Fluid Mechanics, 598:373–382, 2008.
7. Arno Swart, Astrid Manders, Uwe Harlander, and Leo R.M. Maas. Experimental observation of strong mixing due to internal wave focusing over sloping terrain. Dynamics of Atmospheres and Oceans, 50:16–34, 2010.
8. H. Scolan, E. Ermanyuk, and T. Dauxois. Nonlinear Fate of Internal Wave Attrac-tors. Physical Review Letters, 110(23):234501, June 2013.
9. Sibgatullin, E. Ermanyuk, C. Brouzet, and T. Dauxois. Direct numerical simulation of attractors of internal gravity waves and their instability in stratified fluids. In
10. International Summer Course and Workshop on Complex Environmental Turbulent Flows, 2015.
11. Y. Dossmann, B. Bourget, C. Brouzet, T. Dauxois, S. Joubaud, and P. Odier. Mixing by internal waves quantified using combined PIV/PLIF technique. Experiments in Fluids, 57(8):132, August 2016.
12. Nicolas Grisouard, Chantal Staquet, and Ivane Pairaud. Numerical simulation of a two-dimensional internal wave attractor. Journal of Fluid Mechanics, 614:1–14, 2008.
13. C. Brouzet, T. Dauxois, E. Ermanyuk, S. Joubaud, M. Kraposhin, and I. Sibgatullin. Direct numerical simulation of internal gravity wave attractor in trapezoidal do-main with oscillating vertical wall. Proceedings of the Institute for System Program-ming of the RAS, 26(5):117–142, 2014.
14. Ogilvie G. I. Jouve L. Direct numerical simulations of an inertial wave attractor in linearand nonlinear regimes. J. Fluid Mech., 745:223–250, 2014.
15. Christophe Brouzet, Ilias Sibgatullin, Helene Scolan, Evgeny Ermanyuk, and Thierry Dauxois. Internal wave attractors examined using laboratory experiments and 3d numerical simulations. Journal of Fluid Mechanics, 793:109–131, 2016.
16. Christophe Brouzet, Evgeny Ermanyuk, Sylvain Joubaud, Ilias Sibgatullin, and Thierry Dauxois. Energy cascade in internal-wave attractors. EPL (Europhysics Letters), 113(4):44001, 2016.
17. Elistratov S.A., Vatutin K.A., Sibgatullin I.N., Ermanyuk E.V., and Mikhailov E.A. Numerical smulation of internal waves and effects of accumulation of kinetic en-ergy in large aspect ratio domains. Proceedings of ISP RAS, 32(6):200–212, 2020.
18. D. A. Ryazanov, S.A. Elistratov, and M. V. Kraposhin. Visualisation for flows with internal waves attractors. Scientific Visualization, 13(5):113–121, 2021.
19. Jeroen Hazewinkel, Nicolas Grisouard, and Stuart B Dalziel. Comparison of laboratory and numerically observed scalar fields of an internal wave attractor.European Journal of Mechanics-B/Fluids, 30(1):51–56, 2011.
20. Antony Liu and Hsu Ming-Kuang. Internal wave study in the south china sea using synthetic aperture radar (sar). International Journal of Remote Sensing, 25:1261– 1264, 04 2004.
21. S. Cai, J. Xie, and J. He. An overview of internal solitary waves in the south china sea. Acta Oceanologica Sinica, (33):927–943, 2012.
22. Wang G., Zheng Q., Lin M., and Qiao F. Three dimensional simulation of internal wave attractors in the luzon strait. Surv Geophys, 34(11):14–21, 2015.
23. Hel´ene` Scolan, Eugeny Ermanyuk, and Thierry Dauxois. Nonlinear fate of internal wave attractors. Physical review letters, 110(23):234501, 2013.

24. Gostiaux L., Didelle H., Mercier S., and Dauxois T. A novel internal waves generator. Experiments Fluids, 42:123–130, 2007.

25. N.A. Yusoff, Noor Lina Ramli, and Mohd Rusllim Mohamed. Investigation of the potential harnessing tidal energy in malaysia. 10:9835–9841, 01 2015.

26. Riccardo Novo. A preliminay study about methods for harvesting energy from marine resources. PhD thesis, 07 2015.

27. Christine May, Michael Mak, Erica Harris, Mark Lightner, and Justin Vandever. San francisco bay tidal datums and extreme tides study final report. 02 2016.

28. Sara Santamaria-Aguilar, Mark Schuerch, Athanasios Vafeidis, and Silvina Car-retero. Long-term trends and variability of water levels and tides in buenos aires and mar del plata, argentina. Frontiers in Marine Science, 4, 11 2017.

29. Preston Spicer. Tide and Storm Surge Dynamics in Estuaries of Variable Morphology. PhD thesis, 05 2019.

30. D. A. Ryazanov, M. I. Providukhina, I. N. Sibgatullin, and E. V. Ermanyuk. Biharmonic attractors of internal gravity waves. Fluid Dynamics, 56(3):403–412, 2021.

31. M. Mercier, N. Garnier, and T. Dauxois. Analyzing emission, reflection and diffrac-tion of internal waves using the Hilbert transform. In APS Division of Fluid Dynam-ics Meeting Abstracts, page G2, November 2008.

32. Mercier M.and Martinand D., Mathur M., Gostiaux L., Peacock T., and Dauxois T. New wave generation. J. Fluid Mech., 657:308–334, 2010.

33. C. Brouzet, I. N. Sibgatullin, E. V. Ermanyuk, S. Joubaud, and T. Dauxois. Scale effects in internal wave attractors. Phys. Rev. Fluids, 2:114803, Nov 2017.

34. https://nek5000.mcs.anl.gov/.

35. J. Hazewinkel, N. Grisouard, and S. B. Dalziel. Comparison of laboratory and numerically observed scalar fields of an internal wave attractor. European Journal of Mechanics B Fluids, 30:51–56, January 2011.

36. Sibgatullin, E. Ermanyuk, L. Maas, X. Xu, and T. Dauxois. Direct numerical simulation of three-dimensional inertial wave attractors. In2017 Ivannikov ISPRAS Open Conference (ISPRAS), pages 137–143, Nov 2017.

37. Leo R. M. Maas. Wave attractors: linear yet nonlinear. International Journal of Bifurcation and Chaos, 15(09):2757–2782, 2005.

38. Ilias Sibgatullin, Alexandr Petrov, Xiulin Xu, and Leo Maas. On (n,1) wave attrac-tors: Coordinates and saturation time. Symmetry, 14(2), 2022.

39. Chatterjee. An introduction to the proper orthogonal decomposition. Current Science, 28(7):808–817, 2000.

40. John Grue, Didier Clamond, Morten Huseby, and Atle Jensen. Kinematics of ex-treme waves in deep water. Applied Ocean Research, 25(6):355–366, 2003.

41. Tong Jin. Underwater Particle Image Velocimetry (PIV) Measurement of Turbulence

42. Over Mussel Bed in a Deepsite of Lake MichiganTurbulence Over Mussel Bed in a Deepsite of Lake Michigan. A Dissertation Submitted in Partial Fulfillment of the Requirements for the Degree of Doctor of Philosophy in Engineering. 2019.

43. https://www.mbari.org/technology/deeppiv/.

44. Pieter van Breevoort. Experiments on internal wave attractors. PhD thesis, 08 2007.

45. Maxime Brunet, Thierry Dauxois, and Pierre-Philippe Cortet. Linear and nonlinear regimes of an inertial wave attractor. Phys. Rev. Fluids, 4:034801, Mar 2019.

46. S. Boury, I. Sibgatullin, E. Ermanyuk, N. Shmakova, P. Odier, S. Joubaud, L. R.M. Maas, and T. Dauxois. Vortex cluster arising from an axisymmetric inertial wave attractor. Journal of Fluid Mechanics, 926:A12, 2021.